

Improved image-based deformation measurement for geotechnical applications

S.A. Stanier, J. Blaber, W.A. Take, and D.J. White

Abstract: This paper describes and benchmarks a new implementation of image-based deformation measurement for geotechnical applications. The updated approach combines a range of advances in image analysis algorithms and techniques best suited to geotechnical applications. Performance benchmarking of the new approach has used a series of artificial images subjected to prescribed spatially varying displacement fields. An improvement by at least a factor of 10 in measurement precision is achieved relative to the most commonly used particle image velocimetry (PIV) approach for all deformation modes, including rigid-body displacements, rotations, and strains (compressive and shear). Lastly, an example analysis of a centrifuge model test is used to demonstrate the capabilities of the new approach. The strain field generated by penetration of a flat footing and an entrapped sand plug into an underlying clay layer is computed and compared for both the current and updated algorithms. This analysis demonstrates that the enhanced measurement precision improves the clarity of the interpretation.

Key words: image analysis, model tests, particle image velocimetry, digital image correlation.

Résumé : Le présent article décrit et évalue la mise en œuvre récente d'une nouvelle méthode de mesure de déformation basée sur des images et applicable au domaine de la l'ingénierie géotechnique. Cette nouvelle méthode combine une série d'améliorations apportées aux algorithmes et techniques d'analyse d'images spécialement adaptés au domaine de l'ingénierie géotechnique. L'évaluation des performances de cette nouvelle méthode a été réalisée à l'aide d'une série d'images artificielles soumises à des champs de déplacement définis et variant dans l'espace. Une amélioration de la précision des mesures d'un facteur au moins égal à dix est obtenue si l'on utilise la nouvelle méthode plutôt que la méthode la plus souvent employée de la vélocimétrie par images de particules (VIP), et ce pour tous les modes de déformation, y compris les déplacements, rotations et déformations (par compression ou par cisaillement) de corps rigides. Enfin, on se sert d'un exemple d'analyse d'un essai sur modèle en centrifugeuse pour montrer ce que permet de réaliser la nouvelle méthode. Le champ de déformation généré par la pénétration d'un socle plat et d'un bouchon de sable piégé dans une couche d'argile sous-jacente est calculé et comparé aux algorithmes nouveaux et actuels. Cette analyse montre que la plus grande précision des mesures permet d'améliorer la clarté de l'interprétation. [Traduit par la Rédaction]

Mots-clés : analyse des images, essais sur modèle, vélocimétrie par images de particules, corrélation d'images numériques.

Introduction

Measurement of soil deformations in geotechnical models using particle image velocimetry (PIV) techniques (Adrian 1991) — also known as digital image correlation (DIC) (Sutton et al. 1983, 2000) — has become routine experimental practice in many geotechnical research laboratories over the past 15 years (White et al. 2001, 2003; Rechenmacher and Finno 2004; Iskander 2010; Hall 2012; Take 2015). The capabilities of the algorithms and analysis techniques that underpin PIV–DIC have also improved significantly over the same timeframe.

Figure 1a illustrates the typical setup of a geotechnical PIV–DIC analysis for a shallow footing experiment. A wide range of deformation levels are present and accurate and precise displacement data are desired in both the near- and far-field regions of the model. In a typical PIV–DIC analysis, a region of interest (RoI) is first defined within the initial (“reference”) image of the model and populated with a mesh of subsets (or “patches”) of user-defined size. The displacement of these subsets in subsequent (“target”) images is found using one of the approaches illustrated in Fig. 1b. Most freely available PIV–DIC software used for geotech-

nical analyses use some form of cross-correlation to obtain integer pixel displacements followed by subpixel interpolation of the correlation peak (e.g., GeoPIV (White et al. 2003), MatPIV (Sveen and Cowen 2004), PIVlab (Thielicke and Stamhuis 2014), and OpenPIV (Taylor et al. 2010)). In these algorithms the subsets (or patches) are generally not allowed to deform (so-called zero-order deformation).

More sophisticated PIV–DIC algorithms exist, and are introduced later in this paper. They incorporate higher-order subset shape functions (typically first-order, thus allowing displacement gradients across the subsets), image intensity interpolation, and deformation parameter optimization (e.g., Sutton et al. 2000; Pan et al. 2006, 2012). Some of these advances have been incorporated in commercially-available PIV–DIC software (e.g., Vic-2D (Correlated Solutions 2015); LaVision DaVis8 (LaVision 2015); MI-2D (MatchID 2015) although these are not freely available to the academic community and the specific algorithms used are often proprietary. For applications in which small strains are of interest, such as geotechnical modeling and structural monitoring, photogrammetric corrections are often needed to obtain sufficiently accu-

Received 27 May 2015. Accepted 19 October 2015.

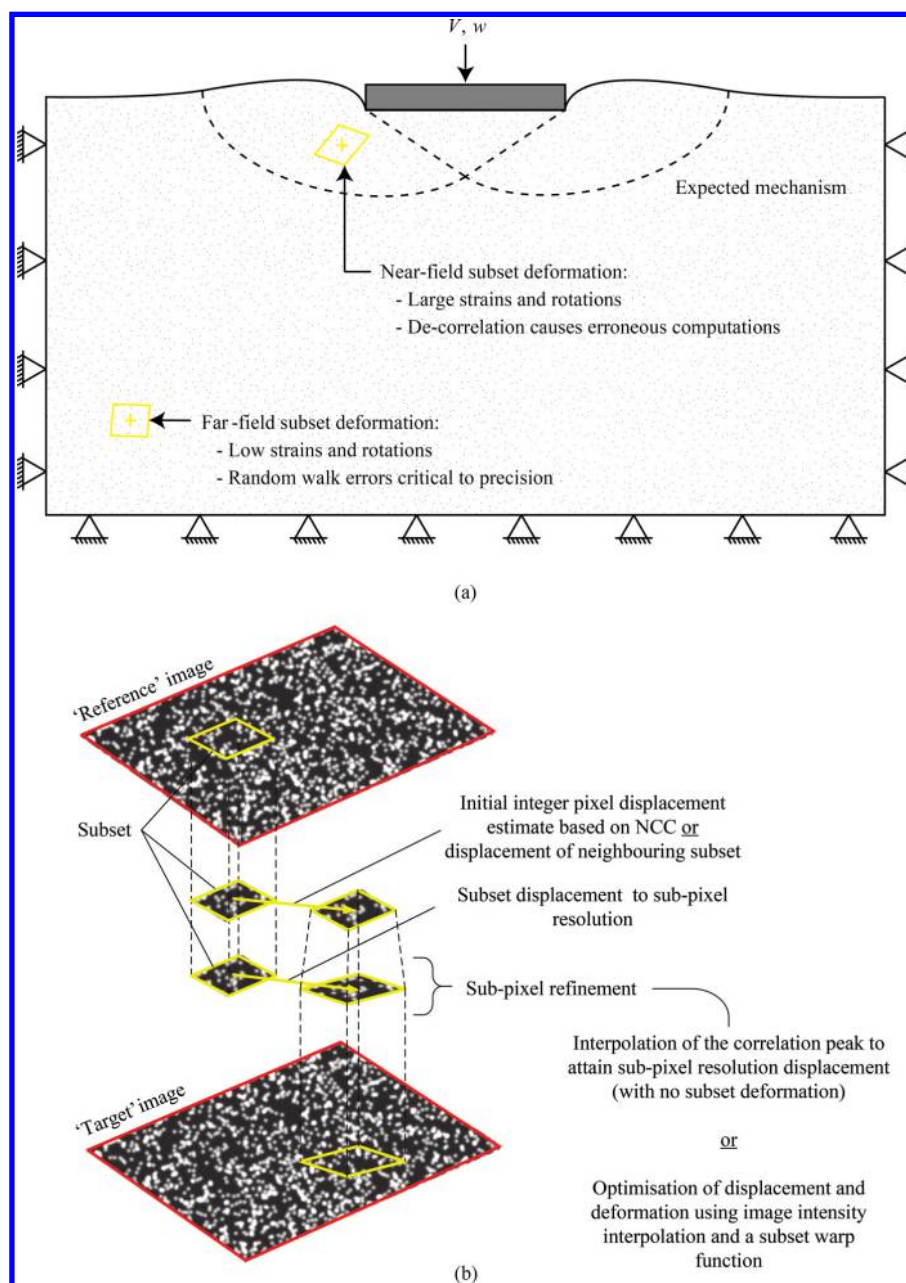
S.A. Stanier and D.J. White. Centre for Offshore Foundation Systems, The University of Western Australia, M053 Fairway, Crawley, WA 6009, Australia.

J. Blaber. Department of Mechanical Engineering, Georgia Institute of Technology, Atlanta, GA, USA.

W.A. Take. Department of Civil Engineering, Queen's University, Kingston, ON, Canada.

Corresponding author: Sam Stanier (email: sam.stanier@uwa.edu.au).

Fig. 1. PIV-DIC analysis overview: (a) typical PIV-DIC scenario with associated causes of error; (b) general overview of the PIV-DIC method. [Colour online.]



rate PIV-DIC results and these correction routines are not usually integrated within either freeware or commercial programs.

The purpose of this paper is to (i) describe the advantages that the more sophisticated genera of PIV-DIC algorithms provide for geotechnical applications involving small and large deformations and (ii) quantify these advantages via benchmark cases using a freely available noncommercial algorithm that is well-suited to the analysis of geotechnical model test images.

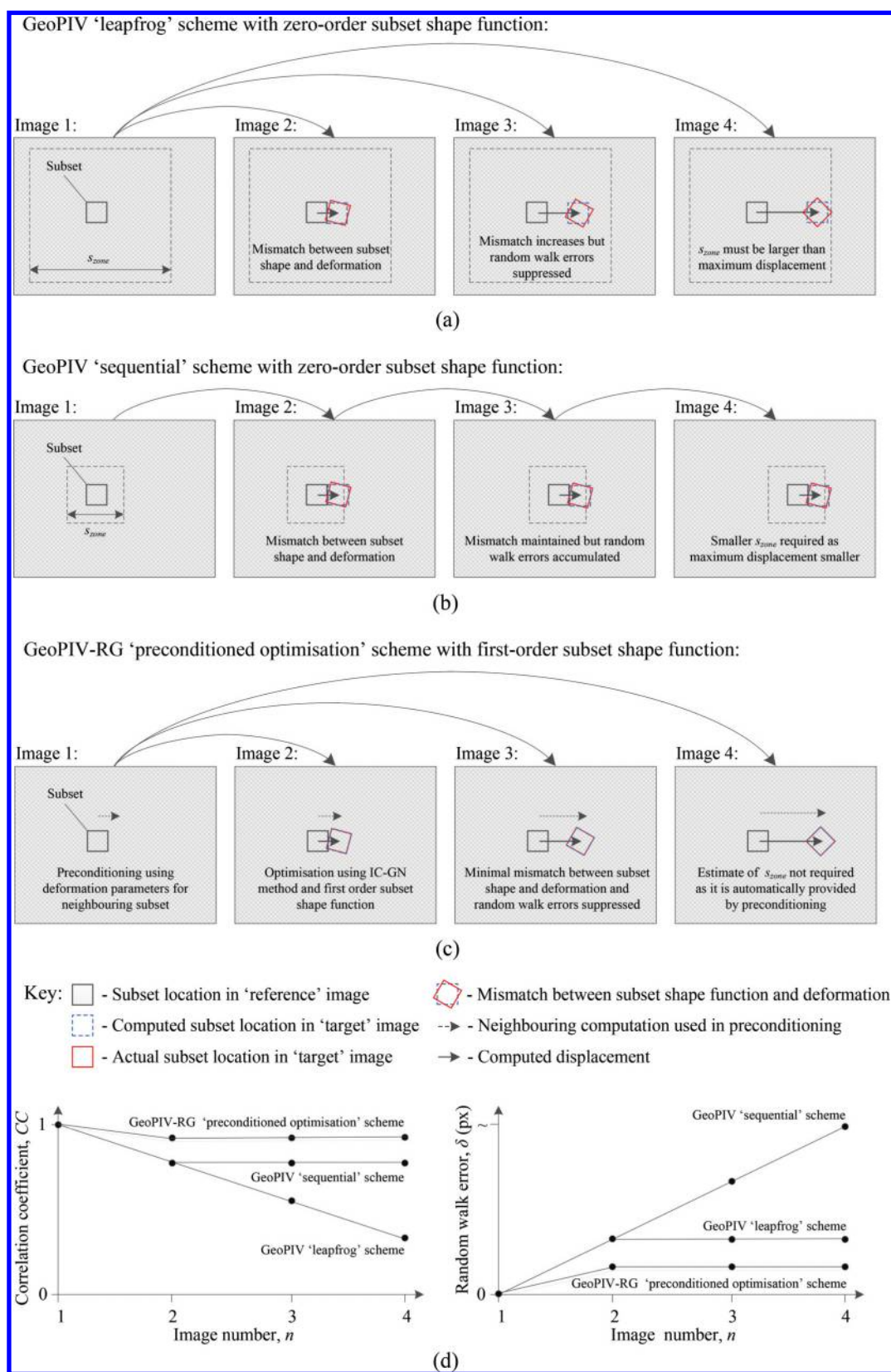
The specific software used for the benchmark cases is referred to as GeoPIV-RG and is an update of the GeoPIV program (which represents the typical algorithms currently used in research, and is described by White et al. (2003)). A brief overview of the computational approach is given first. The comparison is then performed using artificial "soil-like" images subjected to various modes of deformation. Lastly, an example application is given that illustrates the impact this improvement in measurement

precision can have on the interpretation of a classical geotechnical problem.

Computational method

Digital images captured during a geotechnical model test are usually analysed in sequence, starting with an initial reference image. If the reference image is retained as the initial image (the so-called "leapfrog" scheme; see Fig. 2a) then zero-order subsets can suffer a loss of correlation in regions experiencing large deformations (Fig. 2d) due to a mismatch between the subset shape and the deformation being observed. Alternatively, if the reference image is updated after every computation (the so-called "sequential" scheme; see Fig. 2b) to minimize the distortion that would reduce the correlation in the target images, random walk errors are accumulated (White et al. 2003) because the overall

Fig. 2. Overview of (a) “leapfrog”, (b) “sequential”, and (c) “preconditioned optimization” computation schemes alongside (d) schematic plots of the expected evolution of correlation coefficient and random walk errors. [Colour online.]



displacement is being found as the sum of many small displacements, each of which have an associated error (Fig. 2d). Random walk errors can become significant in regions of low deformation when calculating strains from the derivatives of displacement.

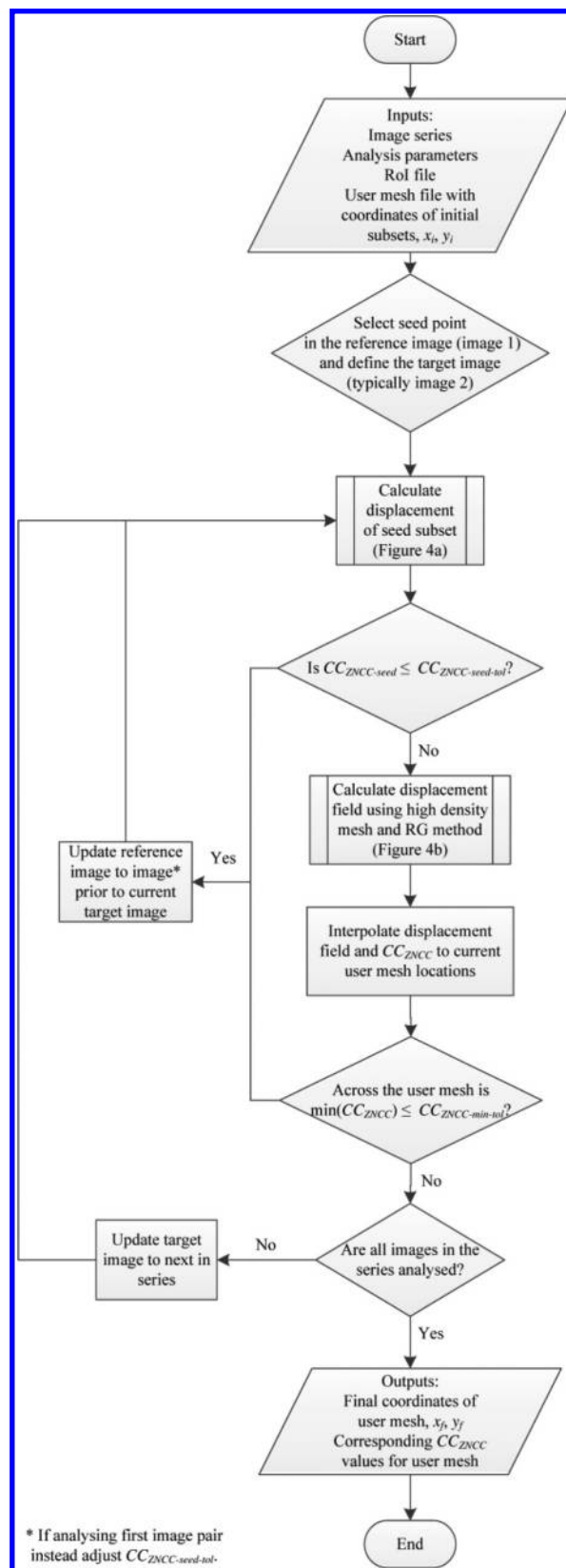
The current version of GeoPIV uses a combination of these two schemes to minimize accumulated random walk errors whilst maintaining tolerable correlations. The number of increments to be performed using the leapfrog scheme prior to updating the reference image (the so-called leapfrog parameter) is manually defined by the user by trial and error guided by the amount of deformation occurring between sequential images. Also, the “search zone” over which the correlation measure is computed for each subset (s_{zone}) is specified by the user in GeoPIV. Unnecessarily large values of s_{zone} lead to computational inefficiency in regions of images experiencing small displacements, therefore small values are preferred. However, the value specified must be larger than the maximum displacement expected to occur between the reference and target images (see Figs. 2a, 2b). Therefore, s_{zone} also cannot be predetermined and requires further trial-and-error refinement to achieve the best balance between accuracy and computational efficiency.

The new implementation presented in this paper avoids the need for trial-and-error refinement of either the leapfrog value or the search zone parameter by following the process illustrated in Fig. 2c for each subset. The overarching framework controlling the computation process is the reliability-guided (RG) method proposed by Pan (2009), as implemented in MATLAB by Blaber et al. (2015) (so the software is referred to as GeoPIV-RG). Each reference subset is allowed to deform using a shape (or warp) function describing first-order deformations in conjunction with image-intensity interpolation techniques to improve the correlation between reference and target subsets via optimization (Schreier and Sutton 2002). After an initial “seed” subset has been analysed, subsequent computations are preconditioned using the results from the previously computed neighbouring subset that has the highest correlation (the so-called “preconditioned optimization” scheme; see Fig. 2c). This approach leads to the definition of a search zone being unnecessary whilst allowing the effective search zone to be the whole image if necessary should the preconditioning process not yield a close match to the optimized solution for any particular subset. The reference image is updated when the correlation coefficient for either the seed or one of the subsets contravenes user-defined thresholds, effectively optimizing the leapfrog parameter. The first-order subset shape function (which allows for linear gradients of displacement across the subset) leads to improved precision and reduced random walk errors (see Fig. 2d) because correlation is better preserved allowing the reference image to be updated less frequently for image sequences experiencing low deformations. The overall programmatic structure of the implementation is summarized by the flowchart shown in Fig. 3.

Seed computation

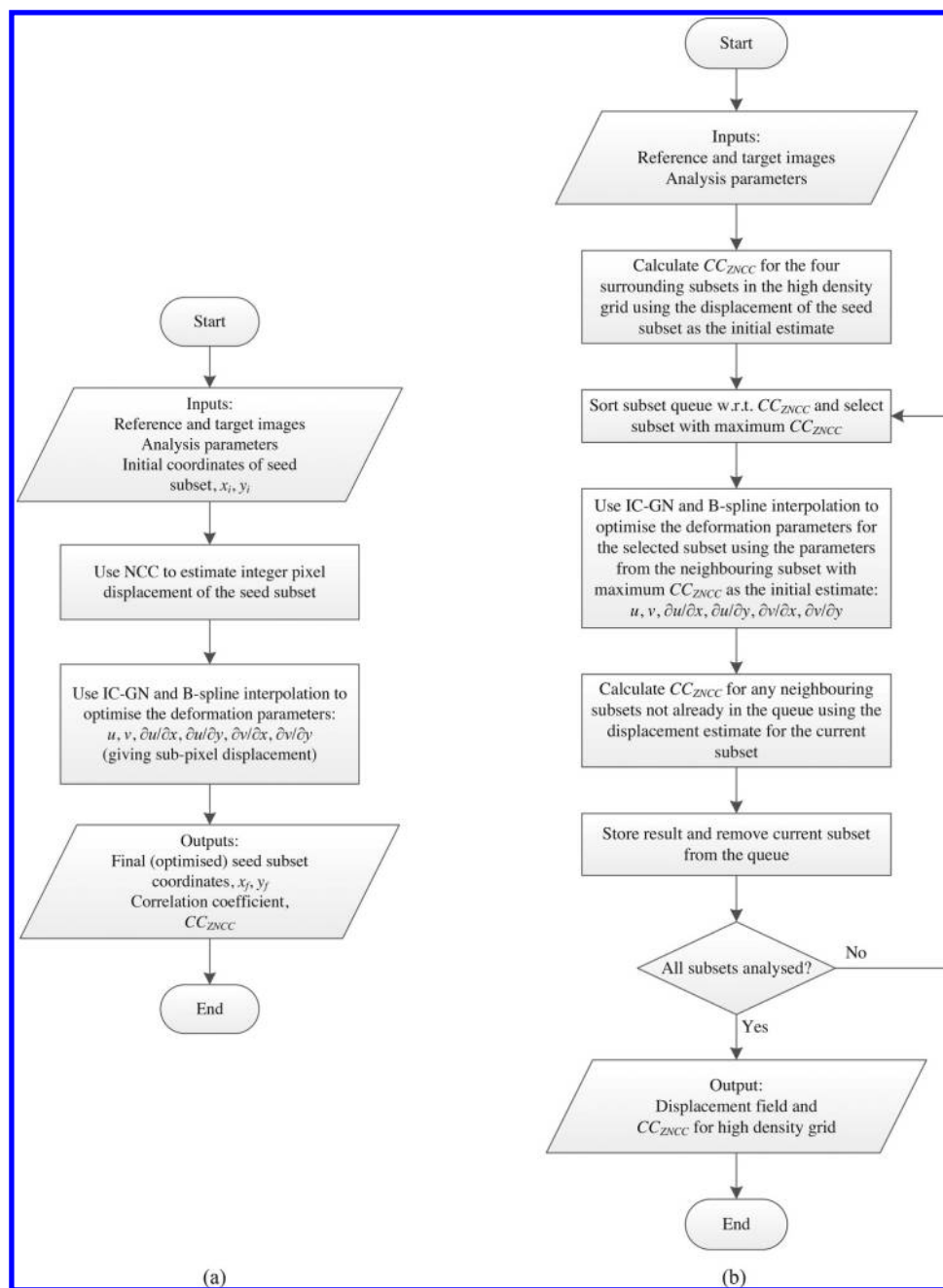
The computation process begins at a selected subset (circular in shape in this instance) from part of the RoI that experiences minimal deformation, meaning that the correlation between the reference and target subset will be high and thus the chances of an incorrectly computed seed occurring will be low. This point is used as a seed from which the RG computation process propagates. The displacement of this subset is computed following the procedure outlined in Fig. 4a. Initially, the displacement of the seed subset is estimated to the nearest integer pixel value using normalized cross correlation (NCC) (Lewis 1995). Next the subset is allowed to deform using a subset shape function (p) that describes a superposition of the first-order subset deformation modes illustrated in Fig. 5 (Pan et al. 2006). The inverse compositional Gauss–Newton (IC–GN) method described by Pan et al. (2013) is used, in

Fig. 3. Flowchart for GeoPIV-RG computations.



combination with bi-quintic B-spline interpolation of the deformed subset pixel intensities (e.g., Cheng et al. 2002) to adjust the subset shape function until the correlation between the reference and target subsets is optimized. The exit criterion for the

Fig. 4. Flowcharts for (a) seed subset and (b) RG subset computation subroutines. IC-GN, inverse compositional Gauss–Newton method.



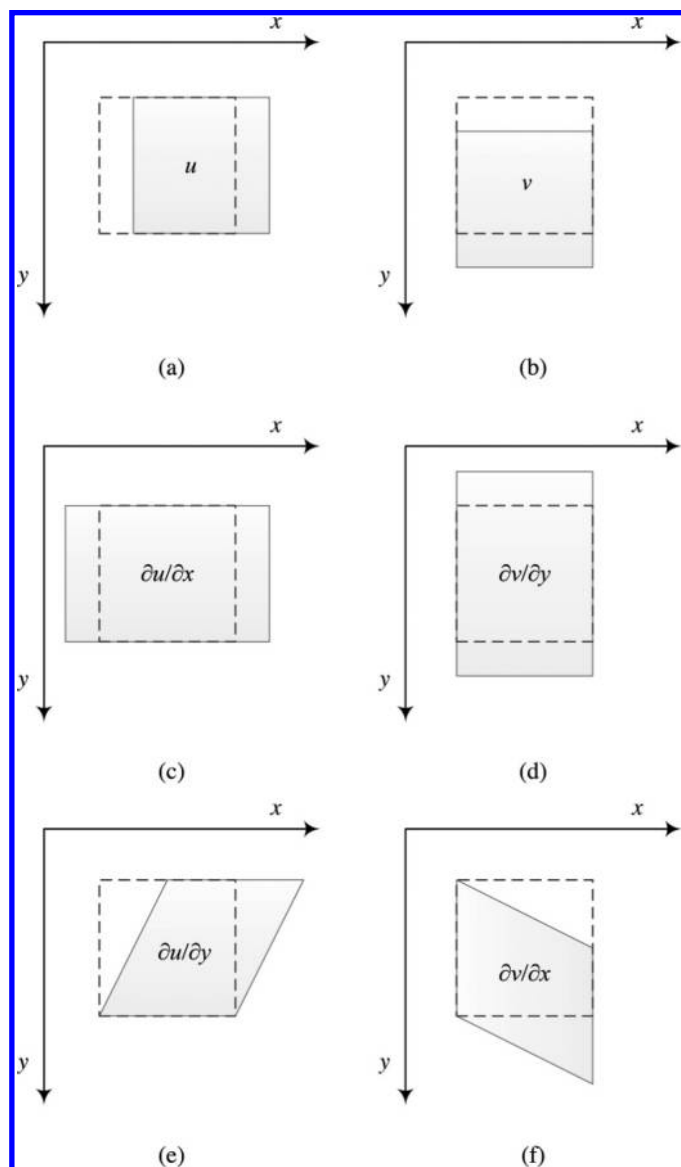
optimization is a user-defined maximum magnitude for the norm of the subset shape function difference vector ($|\Delta \mathbf{p}|_{\max}$) between successive computations (typically 1×10^{-5}) and a maximum number of iterations (\max_{iter}) per subset (typically 50). The zero-normalized cross-correlation correlation coefficient (CC_{ZNCC}) is used to indicate the degree of match where values of 1, 0, and -1 indicate perfect, zero, and inverse correlation, respectively (Pan et al. 2010). The seed computation is deemed successful if the CC_{ZNCC} value is greater than a user-defined limit, $CC_{ZNCC\text{-seed-to-l}}$ (typically 0.9).

Reliability-guided computations

Assuming the seed computation was successful, a high-density grid of subsets is processed using the RG framework outlined in Fig. 4b. Firstly the CC_{ZNCC} of the four subsets surrounding the seed are estimated using the displacement and deformation parameters

for the seed subset as an initial estimate (Zhou and Chen 2012). These four subsets are then placed in a queue of descending CC_{ZNCC} from which the subset with the optimal correlation coefficient is selected first. IC-GN and bi-quintic B-spline interpolation is once again used to optimize the deformation parameters for this subset, then it is removed from the queue. If not already in the queue, the CC_{ZNCC} is computed for the neighboring subsets and those subsets are added to the queue. This process repeats, calculating the displacement and deformation of all of the subsets across the entire RoI. The advantage of the RG framework over the usual processing of subsets across successive rows is three-fold. Firstly, the NCC, which is computationally expensive to determine, is only computed for the seed subset and covers the entire region of interest. Secondly, the subsets with higher correlation coefficients are processed first, and the optimized deformation

Fig. 5. Subset deformation modes considered by the first-order shape function, p : (a, b) displacements and (c–f) displacement gradients. Note: subsets are represented as squares for clarity, but subset shape is arbitrary.



parameters are used to precondition the IC–GN optimization of the neighbouring subsets. Thirdly, as a result of this approach, the need to specify the expected maximum displacement within the displacement field is eliminated.

Reference image updating

Compared to conventional PIV–DIC applications, geotechnical model testing can involve tracking of a larger range of deformations and highly circuitous displacement paths. For example, soil often flows around penetrometers and deeply buried foundations. Unlike fluid mechanics studies, where constitutive relations are not a focus, geotechnical research is concerned with both instantaneous flow fields and also the strain path histories, stress–strain behaviour, and the associated constitutive relations. Additional measures are therefore required to handle the resulting changes in subset appearance, for example due to grain rearrangement, because these lead to a reduction in the subset correlation and cause erroneous displacements to be estimated (known as “wild” vectors). To counter this degradation of correlation, the reference

image can be periodically updated. In earlier versions of GeoPIV the updating interval was specified manually by the user and refined through trial and error (White et al. 2003). An automatic reference image-updating scheme, similar to that proposed by Pan et al. (2012), is used in GeoPIV-RG. After completion of the RG computations for each target image, the CC_{ZNCC} for each subset is compared with a second, slightly relaxed, user-defined limit (typically 0.75) denoted $CC_{ZNCC-min-to1}$. Using a relaxed tolerance on the minimum permissible full field CC_{ZNCC} allows large deformations to occur in certain regions of the model prior to reference image updating. If the CC_{ZNCC} for any subset is less than $CC_{ZNCC-min-to1}$, then the reference image is updated to the target image from the last successful increment, otherwise the current reference image is carried forward.

The RG method is programmed to compute the displacement of regularly gridded subsets. Consequently, an interpolation scheme is required to compute the displacement of the user-defined subset locations from the regularly gridded RG output. Bi-cubic spline interpolation of the output from the RG process achieves this. To safeguard the precision of the measurements during the interpolation process, the subset spacing used in the RG process is reduced relative to that given in the user-defined mesh. For the benchmarking analyses presented in this paper, halving the grid spacing was sufficient to preserve accuracy of the measurements. Due to the computational efficiency of the preconditioned IC–GN optimization process, the computational cost of this four-fold increase in RG computation grid density is minimal. The reference image updating procedure ensures that the updating interval is always optimized. The user can control the frequency of reference image updating indirectly by varying the correlation coefficient tolerances, $CC_{ZNCC-seed-to1}$ and $CC_{ZNCC-min-to1}$, with stricter values resulting in more frequent reference image updating.

Performance comparison

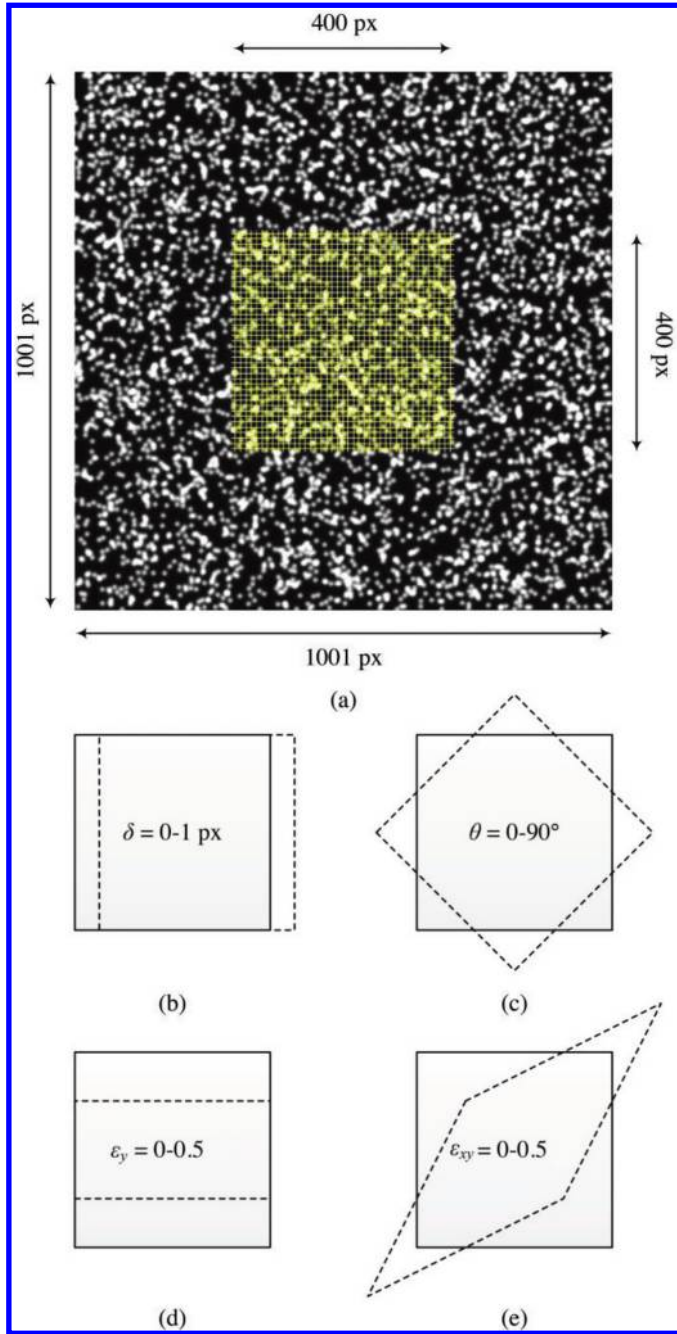
Methodology

The performance of GeoPIV-RG is compared with GeoPIV (described by White et al. 2003 and White et al. 2005), which is widely used in geotechnical research and is typical of the many freely available zero-order algorithms (e.g., MatPIV, PIVlab, and OpenPIV). Therefore the following benchmarking analyses are generally indicative of the improvements in measurement precision that can be attained by incorporating advances in PIV–DIC including first-order subset shape functions, image intensity interpolation, deformation parameter optimization, and automatic reference image updating schemes similar to those described earlier.

Artificial images that represent geomaterials are preferred for such benchmarking as they can be subjected to precisely prescribed deformations and are unaffected by camera-induced lens distortions and camera-target movements (Lee et al. 2012). The images were generated in MATLAB by randomly projecting thousands of white dots onto a black background to subpixel positional resolution. Each white dot is defined by a Gaussian brightness peak centered at a specified location. In this way the location of the dot can be controlled precisely allowing smooth spatially varying displacement fields to be prescribed. The reference artificial image used in all of the artificial benchmarking analyses presented herein is shown in Fig. 6a with the 1681 subset locations marked by yellow crosses in a centrally located zone, of 400×400 pixels (px). This subset population is sufficiently large to generate statistically valid measurements of the error in the image-based displacement measurements. For GeoPIV the side length of the square subsets, L_s , was 45 px, while for GeoPIV-RG the subset diameter, D_s , was taken as 50 px giving comparable total pixels per subset (within ~3%).

The theoretical and measured displacements at the 1681 subset locations were compared for four deformation modes: (i) rigid-body translation, (ii) rigid-body rotation, (iii) vertical strain, and

Fig. 6. Artificial images and imposed deformations: (a) example image and subset locations; (b) rigid-body translation; (c) rigid-body rotation; (d) vertical strain; (e) pure shear strain. [Colour online.]



(iv) pure shear strain as illustrated in Figs. 6b–6e. For rigid-body translation, displacement was applied in 0.025 px increments up to a maximum of 1 px. For the rotation, vertical strain, and pure shear strain analyses, the deformation magnitude imposed was increased over 100 logarithmically spaced intervals up to a maximum of 90° of rotation and 50% strain. The total deformation applied was chosen such that reference image updating was periodically required to validate the efficacy of the full computational scheme. For the analyses performed using the current version of GeoPIV, the reference image was updated manually as infrequently as possible to minimize the summation of random walk errors.

The precision error in the displacement measurements is quantified by the standard error, ρ_{px} , defined as the standard deviation of the difference between the theoretical and calculated subset displacements over the 1681 subsets. It is shown later that this error increases as the deformation of the subset increases. To convert these standard errors to a measure of the precision with which deformations can be determined, the measurement errors (δ) are defined as the error in the measured deformation, for a given level of that deformation mode. An estimate of the random error δ for each mode (rotation, vertical strain, and pure shear strain) can then be defined as

$$(1) \quad \delta_\theta = \tan^{-1}\left(\frac{\sqrt{2}\rho_{px}}{L}\right)$$

$$(2) \quad \delta_{\epsilon_y} = \frac{\sqrt{2}\rho_{px}}{L}$$

$$(3) \quad \delta_{\epsilon_{xy}} = \frac{\sqrt{2}\rho_{px}}{L}$$

where θ , ϵ_y , and ϵ_{xy} denote rotation in degrees, vertical strain, and pure shear strain, respectively, and L is a nominal gauge length in pixels. Each random error δ is estimated for $L = 25$, 250, and 2500 px, which covers the range typically relevant. When viewing a geotechnical model test, the varying deformation throughout the image is of interest, so the relevant gauge length is comparable to the spacing of the subsets, i.e., of the order of 25 px. Alternatively, when viewing a geotechnical element test, at a stage when the deformation is uniform, the gauge length might be significantly larger, i.e., of the order of 2500 px. The δ estimates, combined with a tolerable measurement error, allow the required subset spacing to be identified. Alternatively, they show the image scale (e.g., px/mm) required in a model test to detect a specific level of deformation.

Results

Rigid-body translation

The standard errors, ρ_{px} , in Fig. 7a are ~ 0.006 and ~ 0.001 px for GeoPIV and GeoPIV-RG, respectively, indicating a modest improvement in precision for subpixel displacement measurement for the new methods. Meanwhile, Fig. 7b presents the mean bias error, μ_{bias} (Schreier et al. 2000), which is the mean discrepancy between the actual and measured displacement, for the subpixel rigid-body translation analysis. For GeoPIV, which uses NCC to obtain the integer pixel displacements prior to subpixel interpolation using bi-cubic splines, a significant periodic variation in μ_{bias} is evident for non-integer or non-half-integer displacements. This behaviour is consistent with that reported by Amiot et al. (2013) for PIV-DIC software incorporating bi-cubic interpolation. In contrast, the bi-quintic B-spline interpolation process used in the IC-GN optimization of GeoPIV-RG experiences mean bias errors that never exceed 0.0005 px. This is comparable to the performance reported by Lee et al. (2012) for NCC with bi-quintic B-spline subpixel interpolation and consistent with the best performing PIV-DIC software (with respect to mean bias errors) reported by Amiot et al. (2013) that also incorporated bi-quintic B-spline interpolation. Minimizing bias errors is particularly important if strains are to be derived from the derivatives of displacement fields as periodic bias can lead to erroneous localizations in strain fields.

Rigid-body rotation

Figure 8a shows the evolution of ρ_{px} with rigid-body rotation. GeoPIV accumulates significant errors with increasing rotation because the ability of NCC to accurately track subset displace-

Fig. 7. Rigid-body translation performance: (a) standard error, ρ_{px} , and (b) mean bias error, μ_{bias} , for GeoPIV and GeoPIV-RG. [Colour online.]

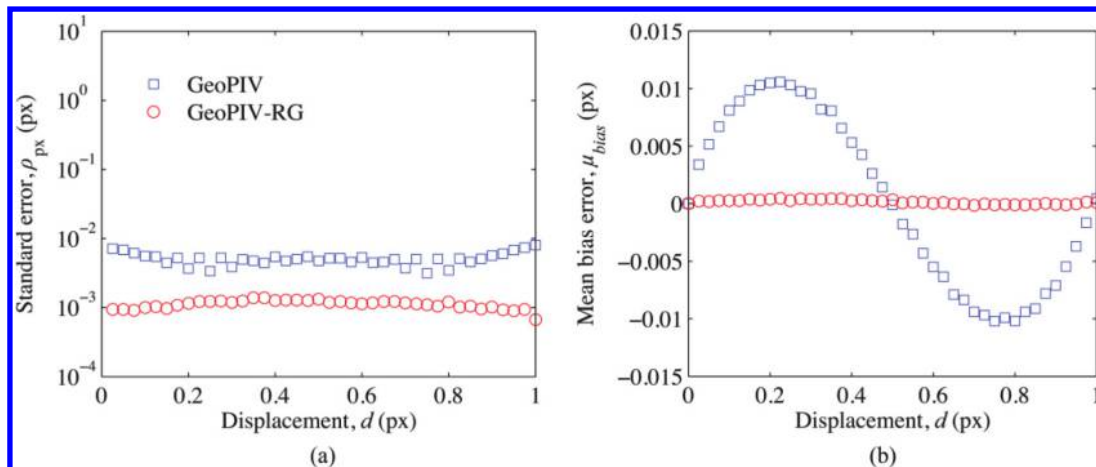
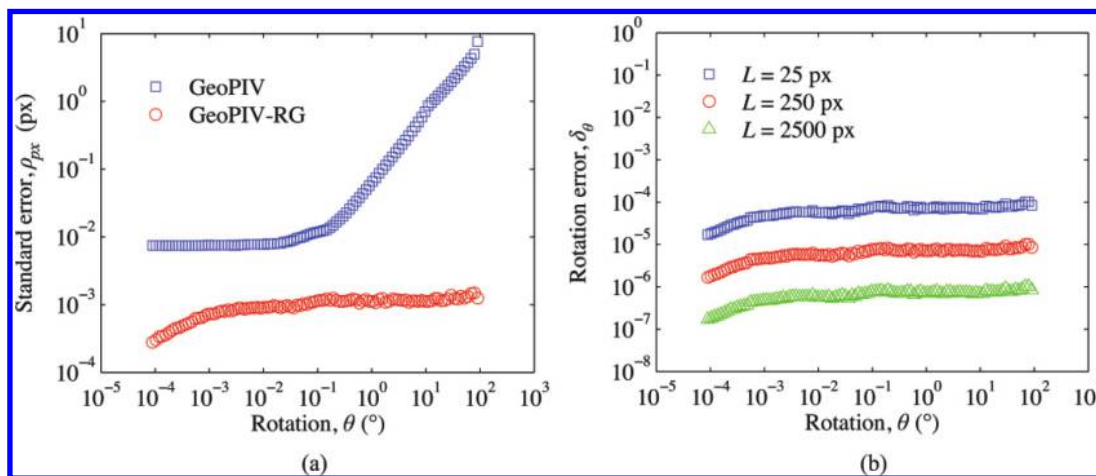


Fig. 8. Rotation performance: (a) standard error for GeoPIV and GeoPIV-RG; (b) effect of gauge length on rotation error, δ_θ , for GeoPIV-RG. [Colour online.]



ments degrades progressively with rotation (Dutton et al. 2014), causing accumulating drift in the displacements. The iterative subset deformation optimization performed by GeoPIV-RG mitigates the degradation of correlation, resulting in a comparatively small precision error of $\rho_{px} < 1/1000$ th of a pixel, irrespective of the rotation magnitude, whilst the mean errors are always less than 1×10^{-4} px. As a result, the rotation error, δ_θ , is approximately constant for rotation magnitudes greater than 1° (Fig. 8b).

The divergence in performance between GeoPIV and GeoPIV-RG observed in Fig. 8 has a profound effect on the abilities of the respective algorithms to measure strain fields because the magnitude of the error is random and not linked to the magnitude of the displacement of the subset. To illustrate this, an additional analysis was performed using the same analysis parameters and artificial images for a horizontal row of subsets spaced at 1 px intervals at increasing distances from the origin of rotation (L_o) up to a maximum of 200 px. For these subsets and for all rotation increments, the rotation angle is the same but the displacement magnitude increases proportionally with the distance from the origin of rotation, as illustrated in Fig. 9a. The resultant error magnitudes (δ_r) were calculated for rotation angles of 0.0° , 0.5° , 1.0° , 1.5° , and 2.0° and are plotted with respect to the distance from the origin of rotation in Figs. 9b and 9d for GeoPIV and GeoPIV-RG, respectively.

From these results it is clear that the error magnitudes and directions are random and unrelated to the distance from the

origin of rotation. However, the error magnitudes are clearly linked to the rotation angle as the error magnitude tends to increase with rotation angle, as is confirmed for GeoPIV in Fig. 9c and GeoPIV-RG in Fig. 9e where the evolution of errors is presented with respect to the rotation angle imposed for subsets located at sections A-A, B-B, and C-C.

For a basic PIV-DIC analysis where vector plots are used to illustrate soil flow mechanisms, the poor performance of GeoPIV for rotation is not necessarily problematic as the large magnitude of the vectors within the soil flow mechanism will mask the errors induced by rotation. However, if strains are derived from the derivatives of the displacement components, the errors become very significant. For example, for a strain element with length $L = 25$ px positioned either side of subset A-A, similarly to eqs. (1)–(3), a generic estimate of the strain error (δ_e) can be taken as follows:

$$(4) \quad \delta_e = \frac{2|\delta_r|}{L}$$

For a rotation angle of 2° , the strain error for GeoPIV is of the order of $\sim 1.2\%$, significantly limiting the ability to plot meaningful strain fields. On the other hand, the strain errors for GeoPIV-RG are less than $\sim 0.012\%$, resulting in a two order of magnitude improvement in strain measurement resolution as a result of the additional degrees of freedom provided by the first-order

Fig. 9. Randomness of rotation performance: (a) artificial image and a row of subset displacements (magnitudes amplified) illustrating the rotation imposed; resultant error, δ_r , as a function of distance from the origin of rotation and rotation angle for (b, c) GeoPIV and (d, e) GeoPIV-RG. Note: Vertical scales are different between (a, b) and (c, d) for clarity. [Colour online.]

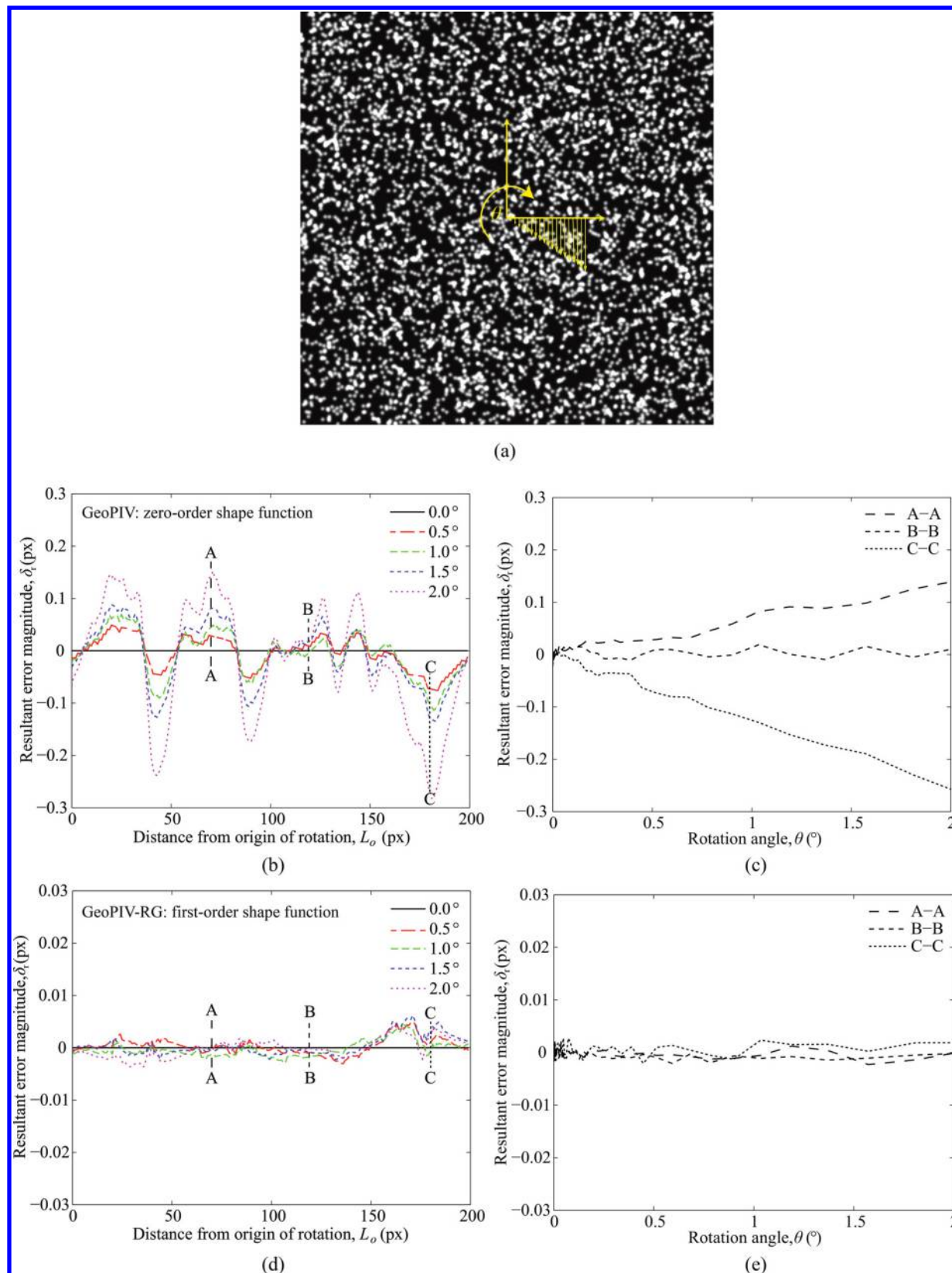


Fig. 10. Vertical strain performance: (a) standard error for GeoPIV and GeoPIV-RG; (b) effect of gauge length on vertical strain error, δ_{ϵ_y} , for GeoPIV-RG. [Colour online.]

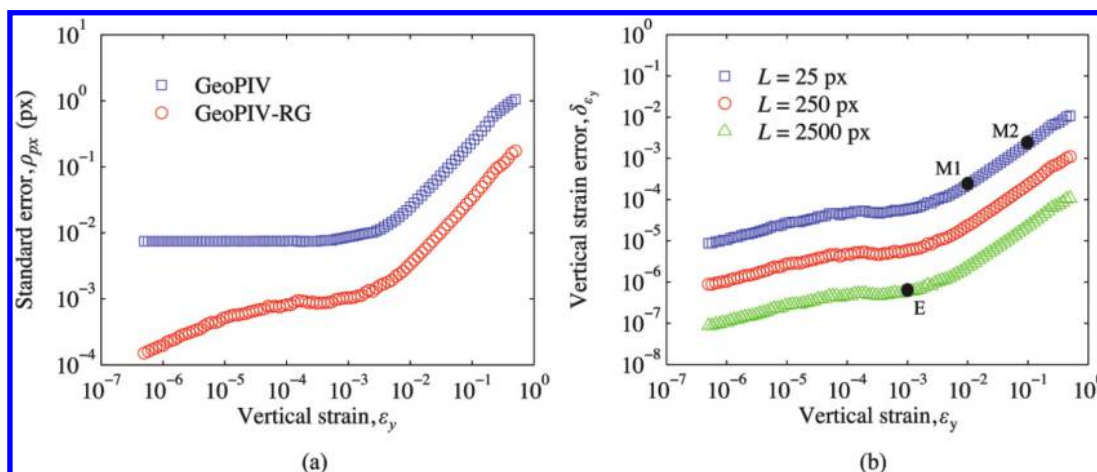
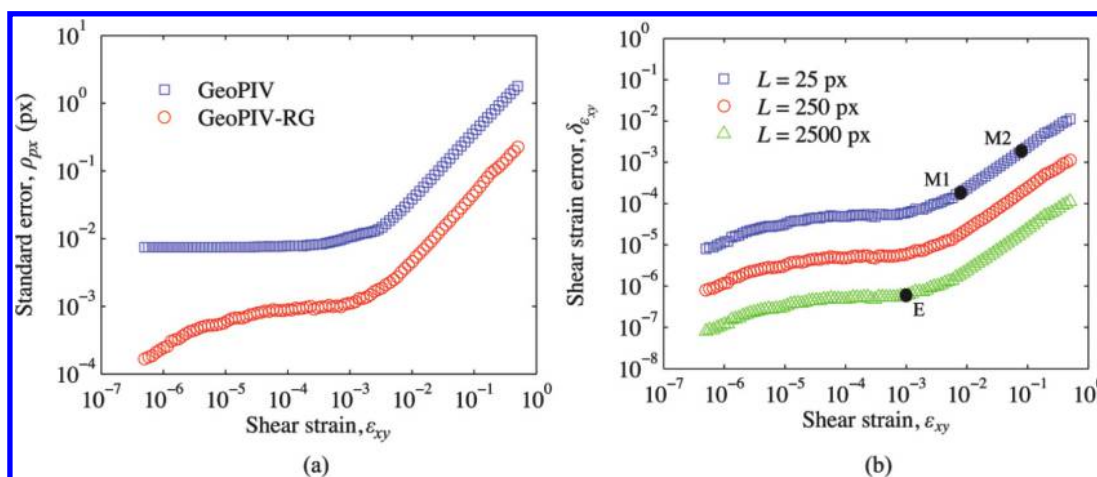


Fig. 11. Shear strain performance: (a) standard error for GeoPIV and GeoPIV-RG; (b) effect of gauge length on shear strain error, $\delta_{\epsilon_{xy}}$, for GeoPIV-RG. [Colour online.]



subset shape function. The impact of this improvement is significant for geotechnical research applications where more than simple instantaneous flow mechanisms are to be observed, such as when gross element distortions are to be monitored through large rotations.

Vertical and shear strain

Figures 10a and 11a illustrate that measurement precision during deformation — either through vertical strain or shear strain — is similar to rotation ($\rho_{px} \sim 1/1000$ px) until $\sim 0.01\%$ or 1% strain, beyond which the precision error rises approximately linearly with strain.

When converted to δ estimates (Figs. 10b and 11b), these results allow the practicality of detecting a given strain level to be assessed. For example, if a model test with a varying deformation is being viewed, then a subset spacing of typically 25 px might apply. In this case, if zones of the model have undergone strains of 1% or 10% (points M1 and M2 in Figs. 10b and 11b), the resulting strain errors would be $\sim 0.025\%$ and $\sim 0.25\%$, respectively (equivalent to a signal-to-noise ratio, SNR, of ~ 40), which is likely to be adequate for producing detailed and smooth deformation fields (e.g., 20 contours of 0.05% or 0.5% up to the maximum of 1% or 10%, respectively). Alternatively, if the application is an element test with uniform deformation, so the gauge length is a larger proportion of the image width — typically 2500 px in width — then at a

strain of 0.1% (100 $\mu\epsilon$) the strain error is $\sim 5 \times 10^{-7}$ (point E in Figs. 10b and 11b) or 0.05 $\mu\epsilon$ (equivalent to an SNR of ~ 2000).

All of these artificial image analyses show that the new approach is at least an order of magnitude more precise than the combination of NCC and bi-cubic spline interpolation method employed by GeoPIV (White et al. 2003), for both small and large deformations.

Example application

To demonstrate the application of the new methodology, images from a model test performed in the drum centrifuge at The University of Western Australia are used. The test involved similar techniques to the work reported by Hu et al. (2014), investigating punch-through of a 30 mm diameter flat footing (at 200g, so equivalent to 6 m diameter at prototype scale) on a 20 mm deep (4 m prototype) sand layer overlying clay. In the experiment, ~ 550 images were recorded at a frequency of 5 Hz using the apparatus described by Stanier and White (2013). Artificial texture was applied to the exposed face of the model at the optimal artificial seeding ratio (ASR) following the procedure proposed by Stanier and White (2013) to maximize the precision of the image-based deformation measurements.

Analyses were performed on the series of images for the underlying clay layer only, using both GeoPIV and GeoPIV-RG with the

Table 1. Computation parameters for example analysis.

Parameter	Value
GeoPIV parameters	
L_s (px)	45 ^a
s (px)	25
s_{zone} (px)	15
Ref. image updating interval	10
GeoPIV-RG parameters	
D_s (px)	50 ^a
s (px)	25
\max_{iter}	50
$ \Delta p _{\text{max}}$	1×10^{-5}
$CC_{\text{ZNCC-seed-tol}}$	0.9
$CC_{\text{ZNCC-min-tol}}$	0.75
Ref. image updating interval	~20

^aSubset sizes chosen to have equivalent area (within ~3%).

analysis settings summarized in Table 1. The time taken by each of the algorithms to perform an analysis is dependent upon a number of factors, including the subset spacing, deformation magnitude, image texture quality, and available processing power. For this particular analysis, GeoPIV-RG performed the computations in ~20% of the time taken by GeoPIV. The total maximum shear strain, ξ (i.e., $\Delta \epsilon_1 - \Delta \epsilon_2$ summed through the deformation), was calculated from the displacement fields following the large strain procedure of White and Bolton (2004).

Figure 12 presents the distributions of ξ after 1D of footing penetration. Significant noise is evident in the results from GeoPIV from summed random walk errors and degradation of correlation due to subset rotation and deformation. In contrast, the analysis generated by GeoPIV-RG has lower noise, as is evident in the regions experiencing small strains. Figure 13 shows a horizontal cross section through both analyses at an initial normalized depth, z/D , of 1.5, presented in terms of both the normalized displacement magnitude and total maximum shear strain. The first-order deformation algorithm of GeoPIV-RG results in smoother spatial variation of both the displacements and strains across the model, compared to the stepped cross section resulting from the zero-order deformation algorithm of GeoPIV.

These enhancements result from the subset deformation optimization capability of GeoPIV-RG as it preserves correlation and precision in regions of large deformation. The reference image also requires updating less frequently (see Table 1), which in turn minimizes random walk errors. These advances create more precise deformation measurements, which unlocks additional potential applications. For example, more detailed verification of constitutive models by extracting element-level responses within model tests, and the quantification of geomaterial behaviour at both smaller strains and higher levels of rotation and deformation than was possible using previous image analysis methods.

Conclusions

This paper has shown that recent advances in PIV-DIC algorithms coupled with photogrammetric correction routines allow improved deformation measurements for geotechnical applications. The algorithms have been incorporated in an update of a commonly used freeware PIV-DIC program. The prior version has been used as a benchmark representing the approaches commonly used in geotechnical physical modelling. The benchmarking used a series of artificial soil-like images subjected to prescribed displacements and deformations. The advanced algorithms are faster and more precise than the simpler zero-order PIV-DIC approach that is widely used and freely available to the research community. Rigid-body displacements can be detected to a precision of ~0.001 px. There is a modest reduction in precision when

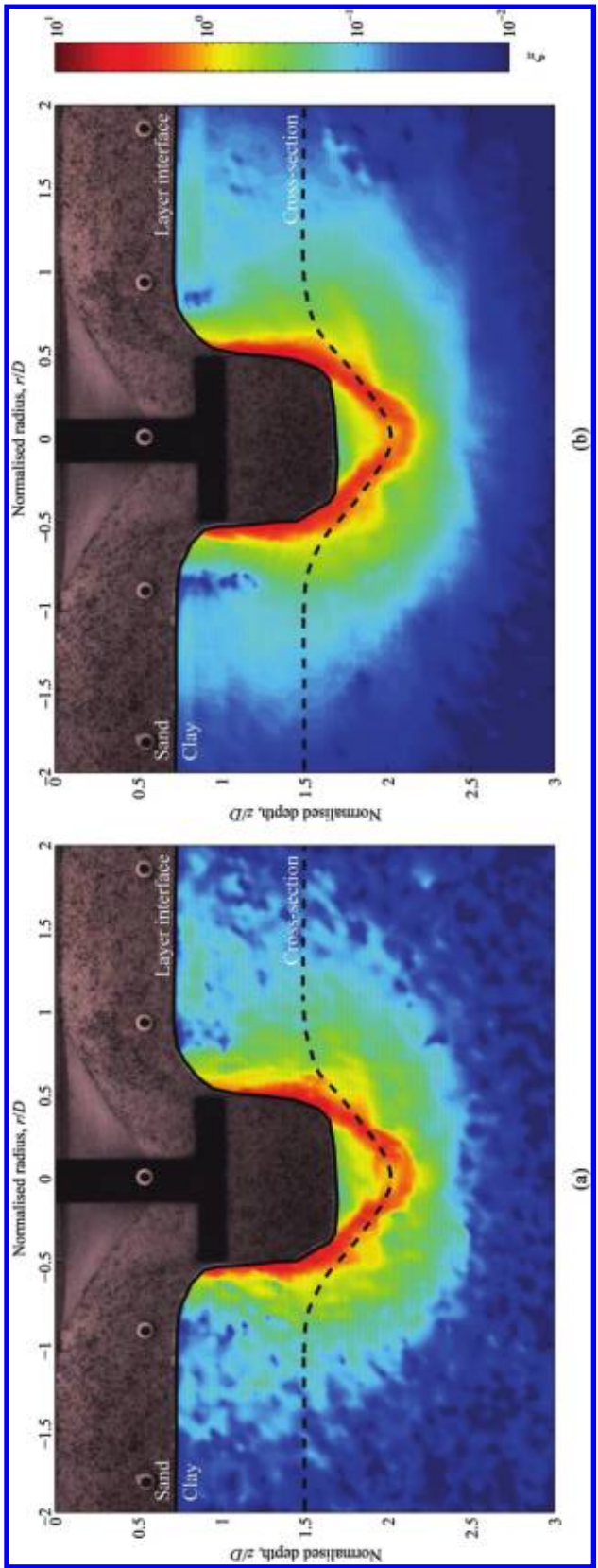
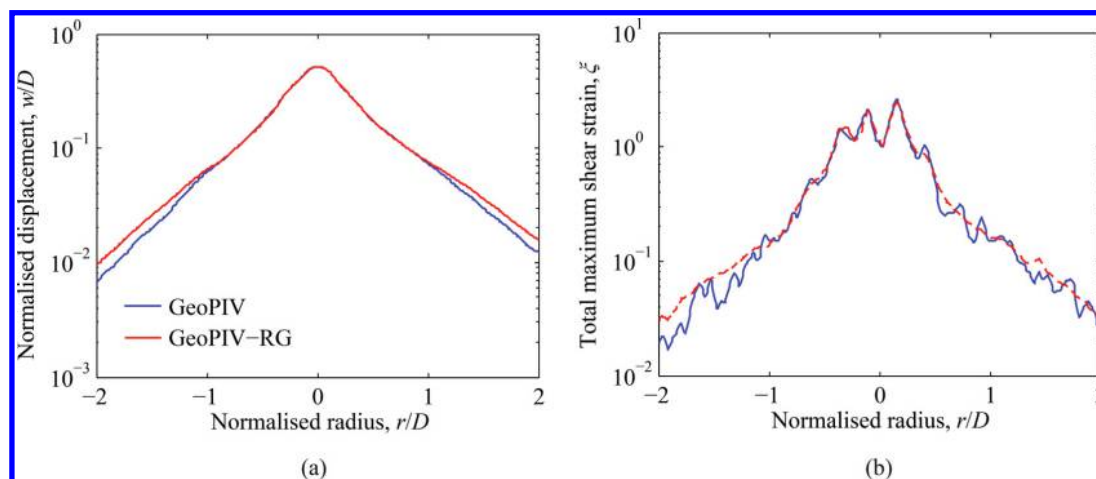


Fig. 12. Example application: flat footing on sand-over-clay; total maximum shear strain, ξ , at 1D penetration using (a) GeoPIV and (b) GeoPIV-RG.

Fig. 13. (a) Normalized displacement, w/D , and (b) total maximum shear strain, ξ , along the cross sections in Figs. 12a and 12b at an initial normalized depth, z/D , of 1.5. [Colour online.]



the tracked soil is deforming. The effect of the gauge length (i.e., the separation of the measurement points) and the level of deformation or rotation on the precision of deformation measurements is quantified. For example, it is shown that when soil elements at close spacing experience rotation in a model test, the new implementation is approximately two orders of magnitude more precise than the existing approach, resulting in significantly less noise in strain fields derived from the derivatives of the displacements. At the other end of the scale, in an element test in which digital images are used to monitor the overall response of the sample (i.e., the gauge length is significantly larger and taken here as 2500 px), the standard error is $\sim 0.05 \mu\epsilon$ at a strain of 0.1%.

An example analysis illustrates the value of the new approach by showing improved measurement of deformations during punch-through of a flat footing on a sand-over-clay stratigraphy. These results demonstrate the benefits of the enhanced measurement precision provided by this software, which is freely available to the geotechnical research community.

Acknowledgements and supplementary information

The research presented here forms part of the activities of the Centre for Offshore Foundation Systems (COFS), currently supported as a node of the Australian Research Council Centre of Excellence for Geotechnical Science and Engineering (grant CE110001009) and through the Fugro Chair in Geotechnics, the Lloyd's Register Foundation Chair and Centre of Excellence in Offshore Foundations, and the Shell EMI Chair in Offshore Engineering (held by the fourth author). The third author is supported by the Natural Sciences and Engineering Research Council of Canada (NSERC) and holds a Canada Research Chair at the GeoEngineering-Centre at Queen's-RMC. The software code and example images relevant to this paper can be downloaded from <http://www.geopivrg.com>.

References

- Adrian, R.J. 1991. Particle-imaging techniques for experimental fluid mechanics. *Annual Review of Fluid Mechanics*, 23: 261–304. doi:10.1146/annurev.fl.23.010191.001401.
- Amiot, F., Bornert, P., Dupre, J.-C., Fazzini, M., Orteu, J.-J., Poilâne, C., Robert, L., Rotinat, R., Toussaint, E., et al. 2013. Assessment of digital image correlation measurement accuracy in the ultimate error regime: main results of a collaborative benchmark. *Strain*, 49: 483–496. doi:10.1111/str.12054.
- Blaber, J., Adair, B., and Antoniou, A. 2015. Ncorr: open-source 2D digital image correlation MATLAB software. *Experimental Mechanics*, 55(6): 1105–1122. doi:10.1007/s11340-015-0009-1.
- Cheng, P., Sutton, M.A., Schreier, H.W., and McNeill, S.R. 2002. Full-field speckle pattern image correlation with B-spline deformation function. *Experimental Mechanics*, 42(3): 344–352. doi:10.1007/BF02410992.
- Correlated Solutions. 2015. The Vic-2D System: technology overview. Available at <http://www.correlatedsolutions.com/vic-2d/>.
- Dutton, M., Take, W.A., and Hout, N.A. 2014. Curvature monitoring of beams using digital image correlation. *Journal of Bridge Engineering*, 19(3): 05013001. doi:10.1061/(ASCE)BE.1943-5592.0000538.
- Hall, S. 2012. Digital image correlation in experimental geomechanics. ALERT Geomaterials Doctoral Summer School 2012. ALERT Geomaterials. pp. 69–102. ISBN: 978-3-00-039683-0.
- Hu, P., Stanier, S.A., Cassidy, M.J., and Wang, D. 2014. Predicting peak resistance of spudcan penetrating sand overlying clay. *Journal of Geotechnical and Geoenvironmental Engineering*, 140(2): 04013009. doi:10.1061/(ASCE)GT.1943-5606.0001016.
- Iskander, M. 2010. *Modelling in transparent soils*. Springer. ISBN-13: 978-3642025006.
- LaVision. 2015. Digital image correlation. Available at <http://www.lavision.de/en/techniques/digital-image-correlation.php>.
- Lee, C., Take, W.A., and Hout, N.A. 2012. Optimum accuracy of two-dimensional strain measurements using digital image correlation. *Journal of Computing in Civil Engineering*, 26: 795–803. doi:10.1061/(ASCE)CP.1943-5487.0000182.
- Lewis, J.P. 1995. Fast normalized cross-correlation. *Industrial Light and Magic*. [Self-published, expanded, and corrected version of: Lewis, J.P. 1995. Fast template matching. In *Proceedings of Vision Interface 95, Canadian Image Processing and Pattern Recognition Society, Quebec City, Que.*, 15–19 May 1995. pp. 120–123.]
- MatchID. 2015. MI-2D: 2D and stereo digital image correlation platform. Available at <http://www.matchidmbc.be/>.
- Pan, B. 2009. Reliability-guided digital image correlation for image deformation measurement. *Applied Optics*, 48(8): 1535–1542. doi:10.1364/AO.48.001535. PMID:19277087.
- Pan, B., Xie, H., Xu, B., and Dai, F. 2006. Performance of sub-pixel registration algorithms in digital image correlation. *Measurement Science and Technology*, 17: 1615–1621. doi:10.1088/0957-0233/17/6/045.
- Pan, B., Xie, H., and Wang, Z. 2010. Equivalence of digital image correlation criteria for pattern matching. *Applied Optics*, 49(28): 5501–5509. doi:10.1364/AO.49.005501. PMID:20885489.
- Pan, B., Wu, D., and Xia, Y. 2012. Incremental calculation for large deformation measurement using reliability-guided digital image correlation. *Optics and Lasers in Engineering*, 50: 586–592. doi:10.1016/j.optlaseng.2011.05.005.
- Pan, B., Li, K., and Tong, W. 2013. Fast, robust and accurate digital image correlation calculation without redundant computations. *Experimental Mechanics*, 53: 1277–1289. doi:10.1007/s11340-013-9717-6.
- Rechenmacher, A.L., and Finno, R.J. 2004. Digital image correlation to evaluate shear banding in dilative sands. *Geotechnical Testing Journal*, 27(1): 13–22. doi:10.1520/GTJ11263J.
- Schreier, H.W., and Sutton, M.A. 2002. Systematic errors in digital image correlation due to undermatched subset shape functions. *Experimental Mechanics*, 42(3): 303–310. doi:10.1007/BF02410987.
- Schreier, H.W., Braasch, J.R., and Sutton, M.A. 2000. Systematic errors in digital image correlation caused by intensity interpolation. *Optical Engineering*, 39(11): 2915–2921. doi:10.1117/1.1314593.
- Stanier, S.A., and White, D.J. 2013. Improved image-based deformation measurement in the centrifuge environment. *Geotechnical Testing Journal*, 36(6): 1–14. doi:10.1520/GTJ20130044.
- Sutton, M.A., Wolters, W.J., Peters, W.H., Ranson, W.F., and McNeill, S.F. 1983. Determination of displacements using an improved digital correlation method. *Image and Vision Computing*, 1(3): 133–139. doi:10.1016/0262-8856(83)90064-1.

- Sutton, M.A., McNeill, S.R., Helm, J.D., and Chao, Y.J. 2000. Advances in two-dimensional and three-dimensional computer vision. *Photomechanics, Topics in Applied Physics*, 77: 323–372. doi:10.1007/3-540-48800-6_10.
- Sveen, J.K., and Cowen, E.A. 2004. Quantitative imaging techniques and their application to wavy flow. In *PIV and water waves*. Edited by J. Grue, P.L.F. Liu, and G.K. Pedersen. World Scientific.
- Take, W.A. 2015. Thirty-Sixth Canadian Geotechnical Colloquium: Advances in visualization of geotechnical processes through digital image correlation. *Canadian Geotechnical Journal*, 52(9): 1199–1220. doi:10.1139/cgj-2014-0080.
- Taylor, Z.J., Gurka, R., Kopp, G.A., and Liberzon, A. 2010. Long-duration time-resolved PIV to study unsteady aerodynamics. *IEEE Transactions on Instrumentation and Measurement*, 59(12): 3262–3269. doi:10.1109/TIM.2010.2047149.
- Thielicke, W., and Stamhuis, E.J. 2014. PIVlab – towards user-friendly, affordable and accurate digital particle image velocimetry in MATLAB. *Journal of Open Research Software*, 2(1): e30. doi:10.5334/jors.bl.
- White, D.J., and Bolton, M.D. 2004. Displacement and strain paths during plane-strain model pile installation in sand. *Géotechnique*, 54(6): 375–397. doi:10.1680/geot.2004.54.6.375.
- White, D.J., Take, W.A., Bolton, M.D., and Munachen, S.E. 2001. A deformation measuring system for geotechnical testing based on digital imaging, close-range photogrammetry, and PIV image analysis. In *Proceedings of the 15th International Conference on Soil Mechanics and Geotechnical Engineering*, Istanbul, Turkey. Balkema, Rotterdam. pp. 539–542.
- White, D.J., Take, W., and Bolton, M. 2003. Soil deformation measurement using Particle Image Velocimetry (PIV) and photogrammetry. *Géotechnique*, 53(7): 619–631. doi:10.1680/geot.2003.53.7.619.
- White, D.J., Take, W.A., and Bolton, M.D. 2005. Discussion of “Accuracy of Digital Image Correlation for measuring deformations in transparent media” by Samer Sadek, Magued G. Iskander, and Jinyuan Liu. *Journal of Computing in Civil Engineering*, 19(2): 217–219. doi:10.1061/(ASCE)0887-3801(2005)19:2(217).
- Zhou, Y., and Chen, Y.Q. 2012. Propagation function for accurate initialization and efficiency enhancement of digital image correlation. *Optics and Lasers in Engineering*, 50(12): 1789–1797. doi:10.1016/j.optlaseng.2012.06.017.

List of symbols

ASR	artificial seeding ratio
CC_{ZNCC}	zero normalized cross-correlation correlation coefficient
$CC_{ZNCC-min-tol}$	full field correlation coefficient tolerance
$CC_{ZNCC-seed}$	seed correlation coefficient
$CC_{ZNCC-seed-tol}$	seed correlation coefficient tolerance
D	diameter
D_s	diameter of GeoPIV-RG subset

d	displacement
L	gauge length
L_o	distance from the origin of rotation
L_s	length of GeoPIV subset
\max_{iter}	maximum number of iterations per subset
NCC	normalized cross correlation
p	subset deformation shape function
$ \Delta p _{\max}$	maximum norm of the shape function difference vector
r	radius
SNR	signal-to-noise-ratio
s	subset spacing
s_{zone}	search zone parameter
u	horizontal displacement
V	vertical load
v	vertical displacement
w	foundation displacement
x	horizontal position
x_f	final horizontal position
x_i	initial horizontal position
y	vertical position
y_f	final vertical position
y_i	initial vertical position
z	depth
δ	measurement error
δ_r	resultant error
δ_e	strain error
$\delta_{e_{xy}}$	shear strain error
δ_{e_y}	vertical strain error
δ_θ	rotation error
ϵ_1	major principal strain
ϵ_2	minor principal strain
ϵ_{xy}	pure shear strain
ϵ_y	vertical strain
θ	rotation angle
μ_{bias}	mean bias error
ξ	total maximum shear strain
ρ_{px}	standard error of displacement measurement in pixels

This article has been cited by:

1. Bing Pan. 2018. Digital image correlation for surface deformation measurement: historical developments, recent advances and future goals. *Measurement Science and Technology* **29**:8, 082001. [[Crossref](#)]
2. S. Mishra, R. G. Robinson. 2018. A combined split-spoon sampler and spherical penetrometer: laboratory trials. *Géotechnique Letters* **8**:2, 118-123. [[Crossref](#)]
3. Pengpeng Wang, Yong Sang, Longtan Shao, Xiaoxia Guo. 2018. Measurement of the deformation of sand in a plane strain compression experiment using incremental digital image correlation. *Acta Geotechnica* **10**. . [[Crossref](#)]
4. Ying Ping Xiao, Hong Cao, Cong Zhai. 2018. Analytical and experimental investigation of a disturbed zone around a pipe in sand. *Journal of the Brazilian Society of Mechanical Sciences and Engineering* **40**:4. . [[Crossref](#)]
5. Belen Ferrer, David Mas. 2018. Parametric Evaluation of Errors Using Isolated Dots for Movement Measurement by Image Cross-Correlation. *Sensors* **18**:2, 525. [[Crossref](#)]
6. P. Ni, I. D. Moore, W. A. Take. 2018. Distributed fibre optic sensing of strains on buried full-scale PVC pipelines crossing a normal fault. *Géotechnique* **68**:1, 1-17. [[Crossref](#)]
7. Zhen Zhang, Feng-Juan Tao, Guan-Bao Ye, Jie Han, Chao Xu, Liu Liu. Physical Models to Investigate Soil Arching Phenomena Under Cyclic Footing Loading Using Transparent Soil 792-801. [[Crossref](#)]
8. Guanxi Yan, Youwei Xu, Vignesh Murgana, Alexander Scheuermann. Application of Image Analysis on Two-Dimensional Experiment of Ground Displacement Under Strip Footing 13-21. [[Crossref](#)]
9. M.R. Abdi, H. Mirzaeifar. 2017. Experimental and PIV evaluation of grain size and distribution on soil-geogrid interactions in pullout test. *Soils and Foundations* **57**:6, 1045-1058. [[Crossref](#)]
10. Marc Elmouttie, Andrew Olsson, Manoj Khanal, Karsten Hoehn, Deepak Adhikary. 2017. A New Feature Based Algorithm for Image Analysis of Deformable Materials for Laboratory Investigations of Slope Stability. *Geotechnical and Geological Engineering* **23**. . [[Crossref](#)]
11. A.F. Cinar, S.M. Barhli, D. Hollis, M. Flansbjer, R.A. Tomlinson, T.J. Marrow, M. Mostafavi. 2017. An autonomous surface discontinuity detection and quantification method by digital image correlation and phase congruency. *Optics and Lasers in Engineering* **96**, 94-106. [[Crossref](#)]
12. Bing Qiuyi Li, Herbert H. Einstein. 2017. Comparison of Visual and Acoustic Emission Observations in a Four Point Bending Experiment on Barre Granite. *Rock Mechanics and Rock Engineering* **50**:9, 2277-2296. [[Crossref](#)]
13. R.N. Tollenaar, L.A. van Paassen, C. Jommi. 2017. Experimental evaluation of the effects of pull rate on the tensile behavior of a clay. *Applied Clay Science* **144**, 131-140. [[Crossref](#)]
14. S. N. Ullah, S. Stanier, Y. Hu, D. White. 2017. Foundation punch-through in clay with sand: analytical modelling. *Géotechnique* **67**:8, 672-690. [[Crossref](#)]
15. Devis Gollin, Wernher Brevis, Elisabeth T. Bowman, Paul Shepley. 2017. Performance of PIV and PTV for granular flow measurements. *Granular Matter* **19**:3. . [[Crossref](#)]
16. Núria M. Pinyol, Mauricio Alvarado. 2017. Novel analysis for large strains based on particle image velocimetry. *Canadian Geotechnical Journal* **54**:7, 933-944. [[Abstract](#)] [[Full Text](#)] [[PDF](#)] [[PDF Plus](#)]
17. X.S. Cheng, G. Zheng, Y. Diao, T.M. Huang, C.H. Deng, D.Q. Nie, Y.W. Lei. 2017. Experimental study of the progressive collapse mechanism of excavations retained by cantilever piles. *Canadian Geotechnical Journal* **54**:4, 574-587. [[Abstract](#)] [[Full Text](#)] [[PDF](#)] [[PDF Plus](#)]
18. Zhibo (Chris) Chen, Kaigang Li, Mehdi Omidvar, Maged Iskander. 2017. Guidelines for DIC in geotechnical engineering research. *International Journal of Physical Modelling in Geotechnics* **17**:1, 3-22. [[Crossref](#)]
19. Yining Teng, Samuel A. Stanier, Susan M. Gourvenec. 2017. Synchronised multi-scale image analysis of soil deformations. *International Journal of Physical Modelling in Geotechnics* **17**:1, 53-71. [[Crossref](#)]
20. Chris A. Murray, Neil A. Hoult, W. Andy Take. 2017. Dynamic measurements using digital image correlation. *International Journal of Physical Modelling in Geotechnics* **17**:1, 41-52. [[Crossref](#)]
21. W. Andy Take, David J. White. 2017. Editorial. *International Journal of Physical Modelling in Geotechnics* **17**:1, 1-2. [[Crossref](#)]
22. J. G. Tom, C. D. O'Loughlin, D. J. White, A. Haghighi, A. Maconochie. 2017. The effect of radial fins on the uplift resistance of buried pipelines. *Géotechnique Letters* **7**:1, 1-8. [[Crossref](#)]
23. Gianluca Zorzi, Matthias Baeßler, Fabio Gabrieli. 2017. Influence of Structural Stiffness on Ratcheting Convection Cells of Granular Soil under Cyclic Lateral Loading. *Procedia Engineering* **175**, 148-156. [[Crossref](#)]

24. Cheng-Cheng Zhang, Hong-Hu Zhu, Bin Shi. 2016. Role of the interface between distributed fibre optic strain sensor and soil in ground deformation measurement. *Scientific Reports* **6**:1. . [[Crossref](#)]
25. F. Gabrieli, L. Corain, L. Vettore. 2016. A low-cost landslide displacement activity assessment from time-lapse photogrammetry and rainfall data: Application to the Tessina landslide site. *Geomorphology* **269**, 56-74. [[Crossref](#)]
26. Sam Stanier, Jelke Dijkstra, Danuta Leśniewska, James Hambleton, David White, David Muir Wood. 2016. Vermiculate artefacts in image analysis of granular materials. *Computers and Geotechnics* **72**, 100-113. [[Crossref](#)]